ONLINE SUPPLEMENT

Quantifying nerve architecture in the mouse and human lung using three-dimensional computational mapping

Gregory D. Scott, Allison D. Fryer, and David B. Jacoby

SUPPLEMENTAL METHODS

Tissue dissection

Harvested tissues were immediately fixed in Zamboni's fixative (MasterTech Scientific, FXZAMPT) overnight at 4°C to minimize neuronal apoptosis. In order to expose epithelial nerves for imaging, airway and gastrointestinal lumina were opened by ventral midline incisions. Airways, from the larynx to the terminal bronchioles, were dissected free of connective tissue and alveoli. In skin samples, hair was manually removed. We avoided enzymatic hair removal (eg. Nair®) in order to minimize epithelial damage. For skin, intestine, and guinea pig, canine, and human airway tissue the submucosa was removed in order to reduce the duration of immunostaining and tissue light scatter, absorbance, and spherical aberration.

Immunohistochemistry

After fixing, immunostaining was performed at 4°C. We avoided dehydration, embedding, tissue sectioning, and two-dimensional image analysis in order to minimize known distortion artifacts of nerve length, nerve surface area, and nerve volume (1-4). Tissues were blocked overnight with 4% Normal Goat Serum, 1% Triton X 100, 5% powered milk in Tris-Buffered Saline pH 7.4, then treated with rabbit polyclonal antiserum against human PGP 9.5 (a nerve-specific protein, Abd Serotec, 7863-0504) for 3 days (5). In order to reduce non-specific binding, tissues were washed in Tris-Buffered Saline (TBS) 5 x 1h then overnight at 4°C followed by overnight immersion in goat anti-rabbit 488 $F(ab')_2$-conjugated secondary antibody (Invitrogen, A-11070). PGP antibodies were identified using the $F(ab')_2$-conjugated secondary antibody because that also reduced non-specific binding and because they penetrate whole tissues better than whole secondary antibodies (6). Tissues were then washed in TBS 5 x 1h and mounted on a charged microscope slide with aqueous mountant (Vectorlabs, H-1200). 1mm coverslip pieces temporarily secured tissues in a lumen-up configuration before mounting. Coverslips (22x22x1.5mm) were weighed down by 100g weights and sealed with Cytoseal 60 (Richard-Allan Scientific, 8310-16). Labeling substance P nerves and

smooth muscle was performed with rat-anti substance P (BD Pharmigen, clone NC1) and mouse anti-alpha smooth muscle actin (Sigma, clone 1A4) primary antibodies followed by goat anti-rat 555 (Invitrogen, A21434) and anti-mouse 647 (Invitrogen, A21235) secondary antibodies.

Generation of deformable surfaces for identifying three-dimensional layer boundaries

Airways are lined with epithelial cells (epithelium) that are separated from airway smooth muscle (in the submucosa) by a basement membrane and connective tissue (lamina propria). Since each harbors distinct nerve populations, it is important in images that capture multiple tissue layers to distinguish the different layers. This is not trivial due to variable thickness and folding. To do this, we developed custom Matlab software to calculate the three-dimensional shape of each tissue layer (Supplemental Fig. 2c online).

Confocal images were resampled in an orthogonal orientation (Supplemental Fig. 2a online) and layer boundaries in 10-15 representative tissue image slices were manually identified using ImageJ software and saved as region files (7) (Supplemental Fig. 2b online). We created Matlab (Mathworks, Natick Massachusetts) software that uses tri-cubic interpolation to calculate the three-dimensional shape of each tissue layer (Supplemental Fig. 2c online). The software loads layer region files and generates three-dimensional matrices of layer surfaces using tricubic interpolation. The software outputs layer information as both serial binary masks and masked image data for use in analysis. The layers identified by Matlab, matched those identified by staining smooth muscle with antibodies to alpha smooth muscle actin, and by autofluorescence of elastin fibers and DAPI staining of nuclei to identify the epithelium (8). This method for identifying epithelium was validated using immunostaining for E-Cadherin, an epithelial cell cadherin involved in cell adhesion (data not shown).

Diffusion Filtering to Identify Nerve Structure

Identification of PGP 9.5 labeled nerves in whole lung is complicated by signal drop off in deep tissue layers, non-neuronal PGP labeling especially in epithelial cells,

auto fluorescence, and variable brightness at the nerve cell membrane making it difficult to determine the edge of the nerve. We mitigated these problems by applying two filtering methods; coherence-enhancing diffusion (CED; demonstration shown in Supplementary Fig. 3 online) and Hessian-based filtering (HBF). Nerve signal is enhanced by these filtering methods which were designed to reduce image noise and enhance edges, linear shapes, and tubular structures. Coherence-enhancing diffusion (CED) is an anisotropic diffusion filtering method for filtering linear structures such as nerves (9). A three-dimensional diffusion tensor is adapted to linear structures allowing for elongated smoothing kernels along edges. CED has been used in software designed for diffusion tensor magnetic resonance imaging, microtubule identification in electron microscopy tomographs, analysis of fabrics, and fingerprint analysis. Our second approach was originally developed by Frangi to identify blood vessels in angiograms and uses the Hessian matrix of second derivative image data to calculate curvature (10). We used open-source Matlab implementations of CED and Frangi filter made available by D.J. Kroon (http://www.mathworks.com/matlabcentral/fileexchange/24409-hessian-based-frangi-vesselness-filter). Diffusion time and Gaussian sigma parameters were adjusted for signal intensity variation due to tissue thickness.

Bit-mapped Masks from Tessellated Nerve Map

Imaris exports VMRL standard vector graphics for generating bit-mapped masks from tessellated data. Although not used in the current study, we adapted software for 3D printing (http://www.freesteel.co.uk) to create masks from nerve map data (data not shown). These (bitmapped) masks will be useful in future 3D co-labeling studies. For figures 3 and 4, the total data set represented 7+3 locations and six mice, but space within the figures allowed for only 5 locations, one image and computer map per location at top, side, and lateral views. Representative images were selected systematically where images were ensured to come from different mice and nerve quantification was close to the group mean value rather than a hand-picked image showing a maximum or minimum nerve length and branching value.

Comparison of Computer Nerve Mapping Analysis to Manual Human Quantification

Manual quantification of branchpoints in three-dimensional images of airway nerves was compared to our computer nerve mapping approach. Three blinded human observers were given six 63x image stacks and branchpoints were counted as the convergence of three or more neurites or “branches”. Branchpoints were designated as “out-of-plane” if a branch was oriented in a different direction to the original image (ie not parallel to the objective (x,y) field of view). Conversely, branchpoints designated as “in-plane” contained three branches viewable within the non-rotated image. Human counters were given a priori instructions on viewing non-rotated (orthogonal) images and rotated (oblique) images, and shown examples of in-plane and out-of-plane branches.

Nerve length was compared to two forms of manual quantification. In six 63x image stacks, nerves were manually traced in ImageJ as connected line segments in 3D image data (“3D Manual”) or flattened 2D maximum intensity projections of the 3D data (“2D Manual”). In both the 2D and 3D manual approaches, nerve length was calculated as the sum of Cartesian lengths for each tracing segment.

References

E1. Muhlfeld C, Papadakis T, Krasteva G, Nyengaard JR, Hahn U, Kummer W. An unbiased stereological method for efficiently quantifying the innervation of the heart and other organs based on total length estimations. *Journal of applied physiology* 2010;108(5):1402-1409.
E2. Hanani M, Ermilov LG, Schmalz PF, Louzon V, Miller SM, Szurszewski JH. The three-dimensional structure of myenteric neurons in the guinea-pig ileum. *J Auton Nerv Syst* 1998;71(1):1-9.
E3. Karaosmanoglu T, Aygun B, Wade PR, Gershon MD. Regional differences in the number of neurons in the myenteric plexus of the guinea pig small intestine and colon: An evaluation of markers used to count neurons. *The Anatomical record* 1996;244(4):470-480.
E4. Freytag C, Seeger J, Siegemund T, Grosche J, Grosche A, Freeman DE, Schusser GF, Hartig W. Immunohistochemical characterization and quantitative analysis of neurons in the myenteric plexus of the equine intestine. *Brain research* 2008;1244:53-64.
E5. Thompson RJ, Doran JF, Jackson P, Dhillon AP, Rode J. Pgp 9.5--a new marker for vertebrate neurons and neuroendocrine cells. *Brain research* 1983;278(1-2):224-228.
E6. Brandon C. Improved immunocytochemical staining through the use of fab fragments of primary antibody, fab-specific second antibody, and fab-horseradish peroxidase. *The journal of histochemistry and cytochemistry : official journal of the Histochemistry Society* 1985;33(7):715-719.
E7. Abramoff MD, Magalhaes PJ, Ram SJ. Image processing with imagej. *Biophotonics International* 2004;11(7):36-42.
E8. Thiberville L, Moreno-Swirc S, Vercauteren T, Peltier E, Cave C, Bourg Heckly G. In vivo imaging of the bronchial wall microstructure using fibered confocal fluorescence microscopy. *Am J Respir Crit Care Med* 2007;175(1):22-31.
E9. Weickert J. Coherence-enhancing diffusion filtering. *Int J Comp Vis* 1999;31(2):111-127.
E10. Frangi AF, Niessen WJ, Nederkoorn PJ, Bakker J, Mali WP, Viergever MA. Quantitative analysis of vascular morphology from 3d mr angiograms: In vitro and in vivo results. *Magnetic resonance in medicine : official journal of the Society of Magnetic Resonance in Medicine / Society of Magnetic Resonance in Medicine* 2001;45(2):311-322.

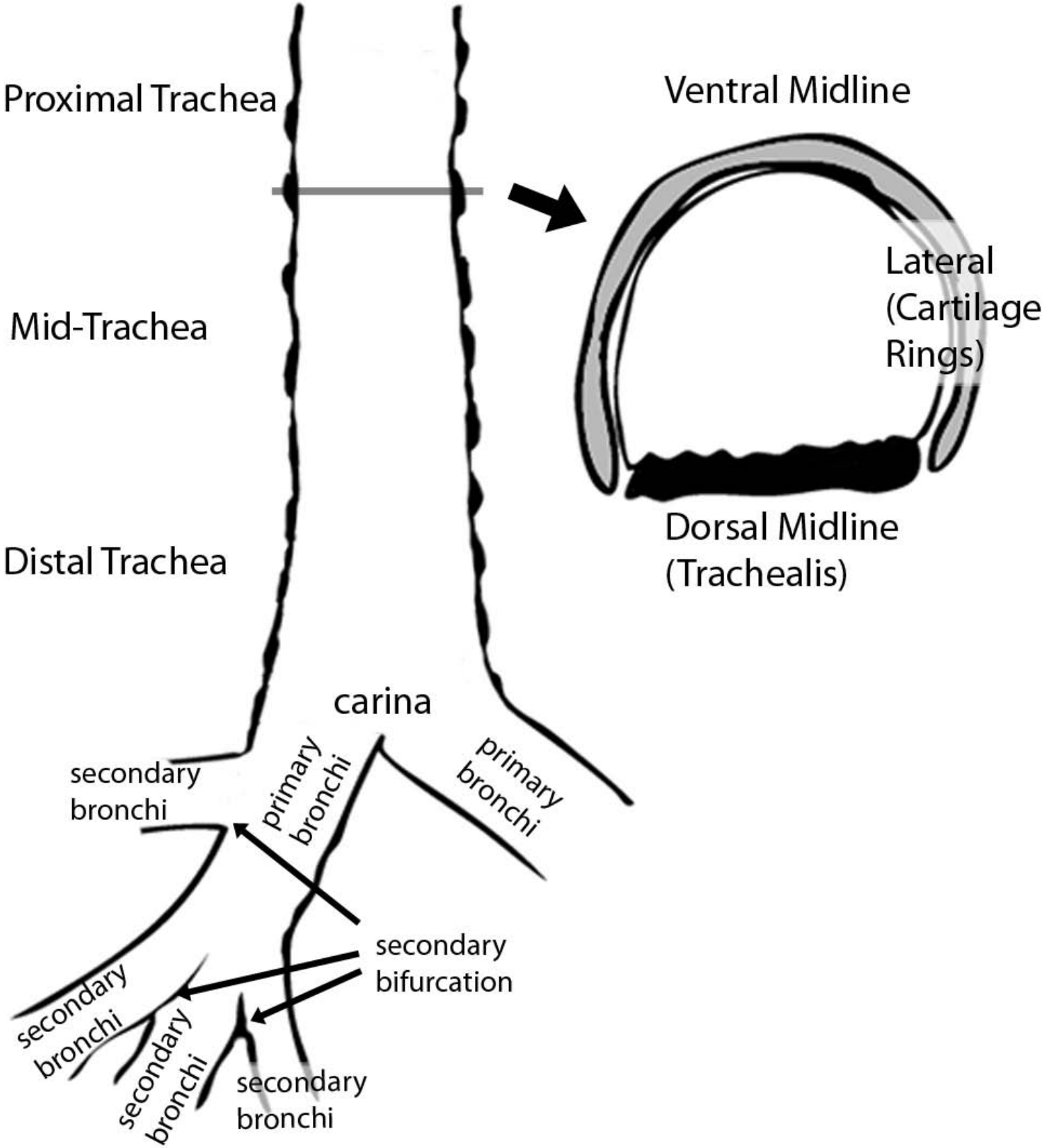

Supplementary Figure 1. Airway Regions in the Mouse with Epithelial Nerves. The trachea was divided into three even proximal-to-distal and three dorsal-lateral-ventral regions. The carina (first airway division) and secondary bifurcations were quantified separately from distal trachea/primary bronchi and primary bronchi/secondary bronchi respectively.

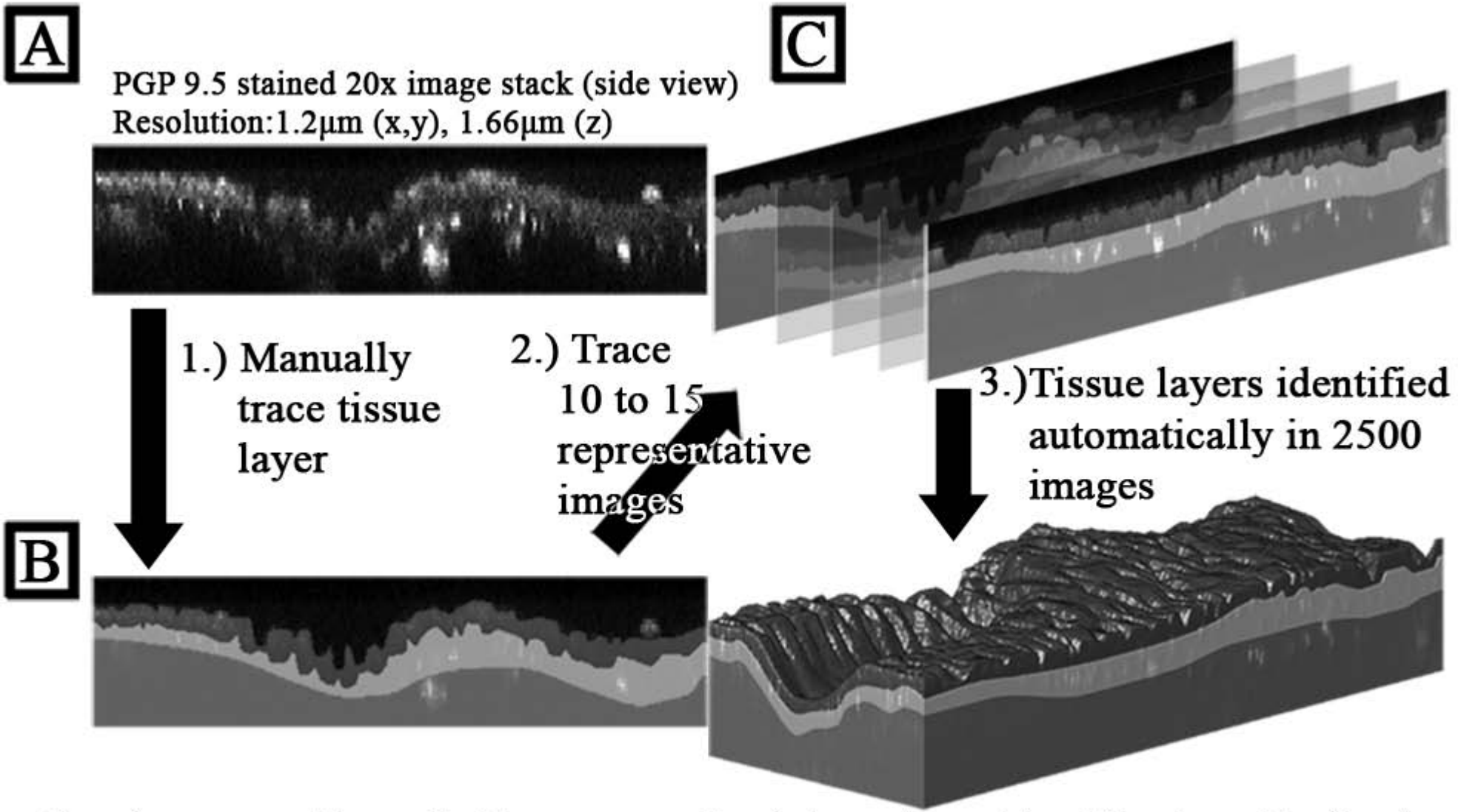

Supplementary Figure 2. Computer assisted tissue layer identification. Confocal image stacks of airway tissue are rotated (A) to a lateral view and tissue layers are manually identified (B) in 10-15 representative images. A custom program generates (C) malleable surface for the: **epithelium** **lamina propria** **submucosa**

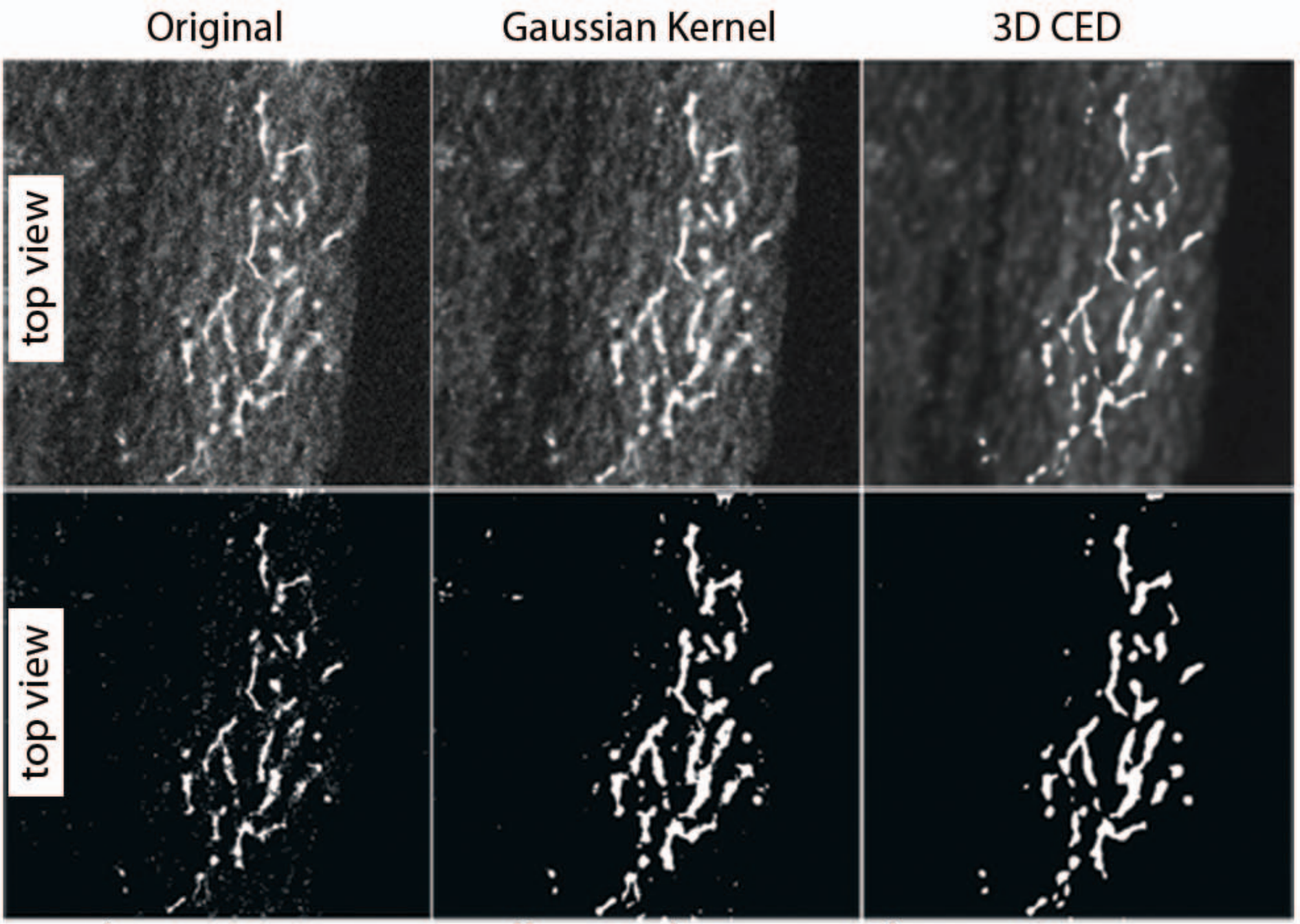

Supplementary Figure 3. Diffusion Filtering to Enhance 3D Nerve Images. (top row) Image data before and after pre-processing filters. (bottom row) binary mask after intensity threshold. (left) Slice of raw 3D nerve data with brightness increased to show image noise. (middle) Slice of gaussian filtered (1 pixel radius) 3D nerve data. (right) Slice of 3D nerve data filtered with 3D coherence-enhancing diffusion. Lower row shows improved identification of nerve signal using coherence-enhancing diffusion.

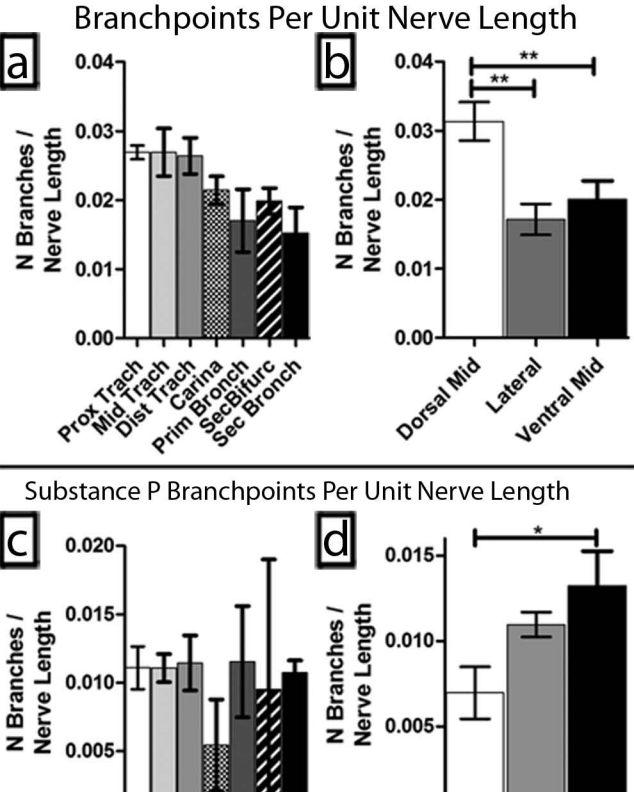

Supplementary Figure 4. Changes in Nerve Branching Evaluated By Adjusting for Nerve Length. Nerve branchpoints were divided by nerve length for all epithelial nerves (a,b) and the substance P subpopulation (c,d). Overall nerve branching per unit nerve length decreased proximal-to-distal (a) and dorsal-to-lateral/ventral (b) but proximal-to-distal was non-significant for post-test comparison of each location (b). Unlike overall nerves, substance P branching per unit length increased dorsal-lateral-ventral (d) but not proximal-to-distal (c). n=6 * $p < 0.05$, ** $p < 0.01$

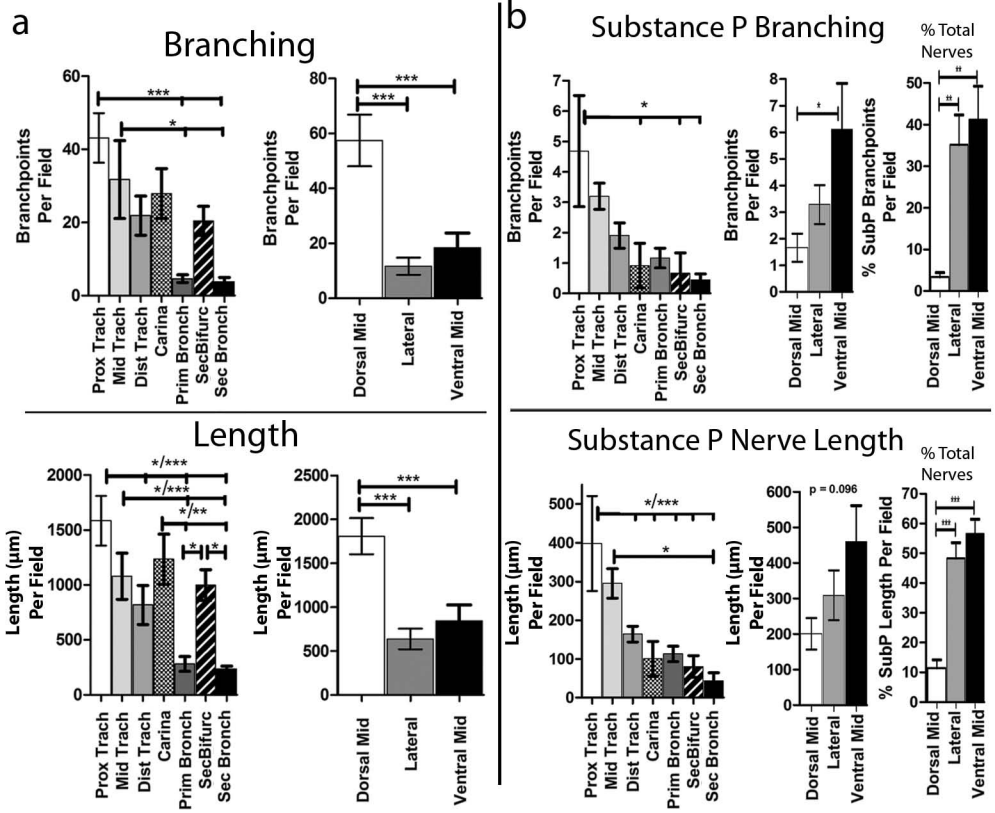

Supplementary Figure 5. Quantification of Airway Epithelial Nerves Not Normalized to Epithelial Volume (a) Nerve length and number of branchpoints per high-powered field was quantified by the computer (n=6). Nerve length and branching decreased proximal-to-distal with regional increases at airway bifurcations. Nerve length and branching decreased from the dorsal midline to lateral and ventral positions in the trachea. (b) Substance P nerve length and branching was also quantified by the computer (n=6). Unlike total epithelial nerves identified by PGP 9.5, substance P nerve length and branching increased from dorsal to lateral and ventral positions. This was also seen when substance P nerve length and branching was calculated as a percentage of total nerve length and branching. Unlike total nerves, substance P nerve length and branching also did not increase at airway bifurcations. See Supplementary Figure 1 for airway region diagram. * $p < 0.05$, ** $p < 0.01$, *** $p < 0.001$.

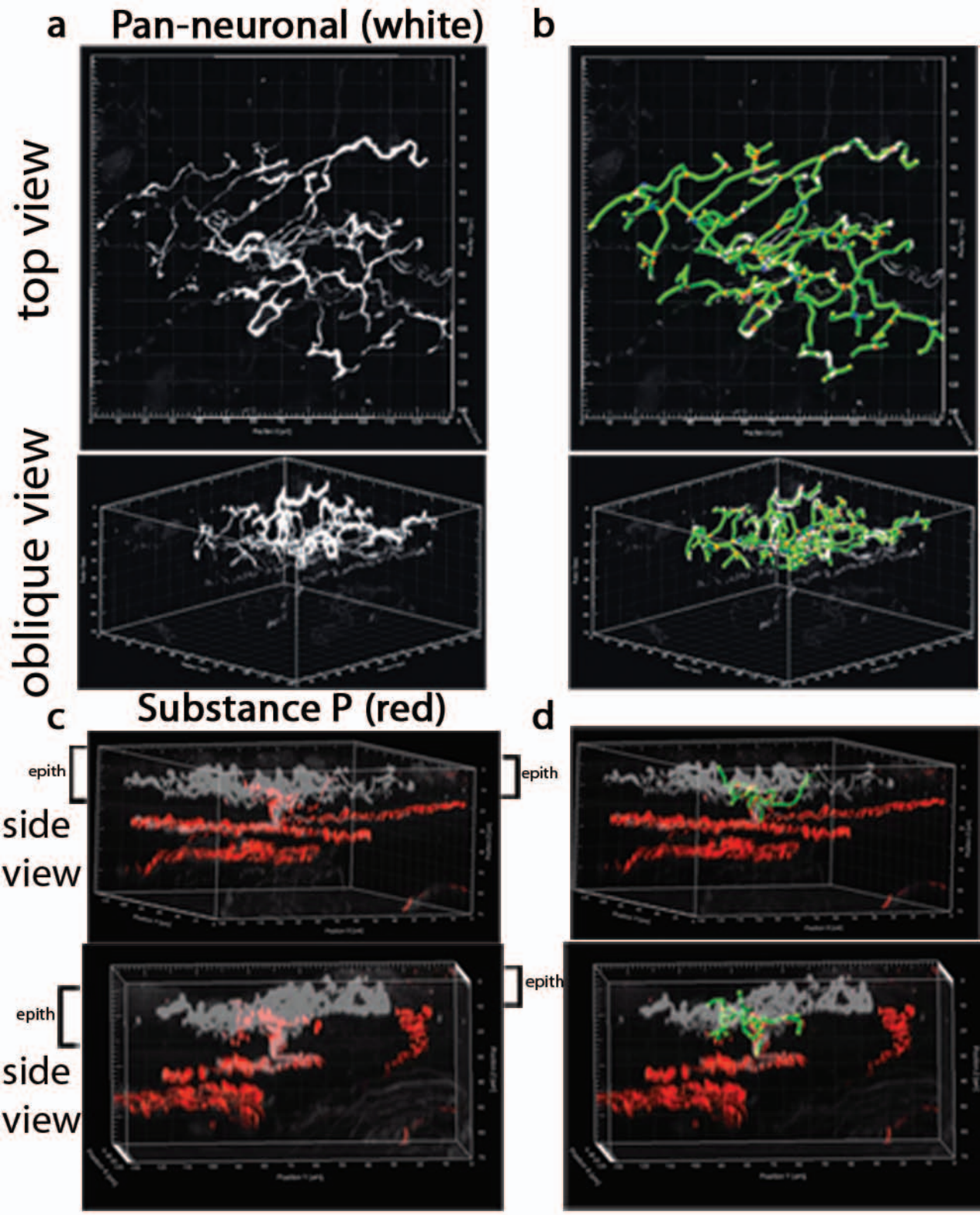

Supplementary Figure 6. Computer Mapping Epithelial Nerves and the Substance P Subpopulation. (a-d) Lateral projections of an epithelial nerve patch containing a substance P subpopulation. (a) All nerves (white) were labeled using the pan-neuronal marker, PGP 9.5, and a sub-population (red) expressed substance P. (b) Overlay of raw image data and computer map of total epithelial nerves (green). (c) Substance P subpopulation (red) overlaid with total nerves (white-transparent) and (d) shown with the substance P nerve map (green).

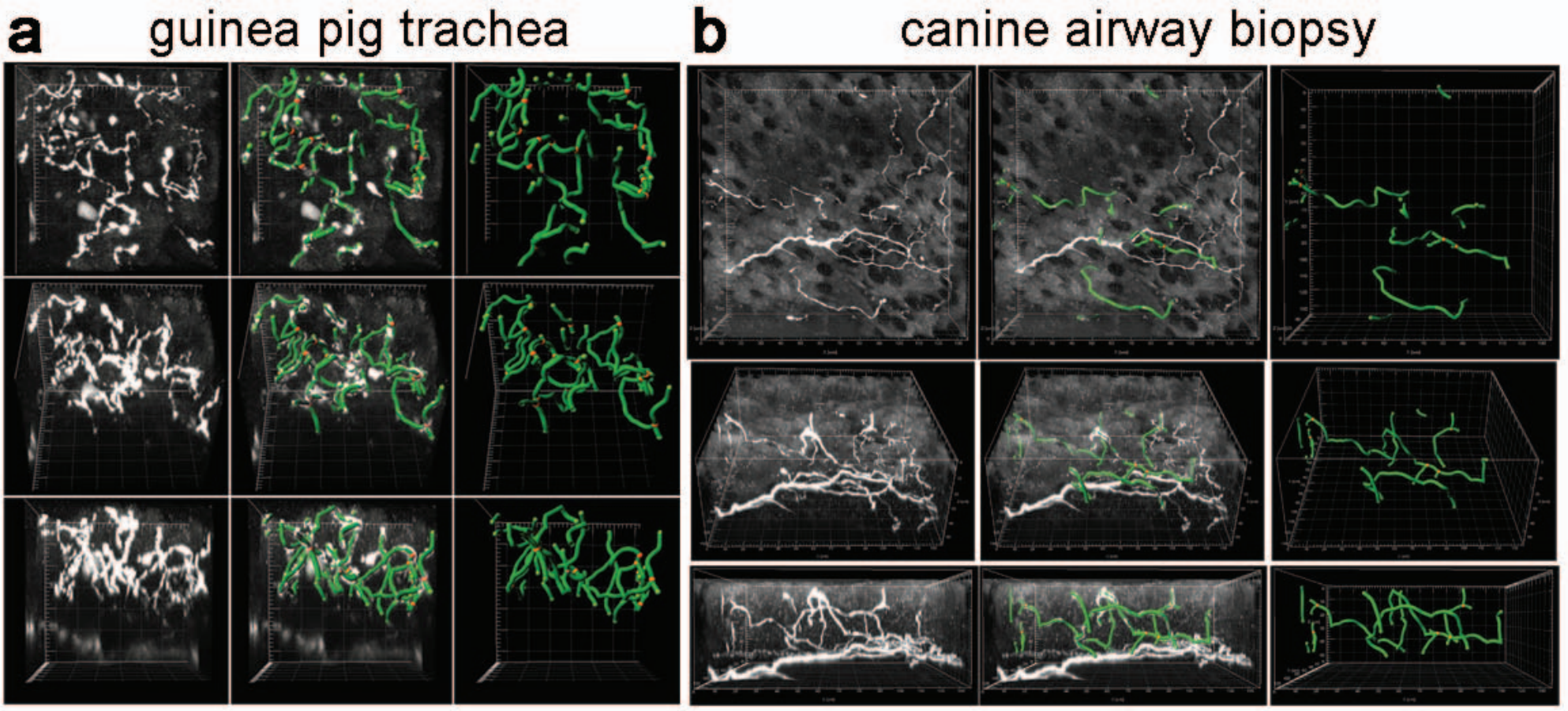

Supplementary Figure 7. Epithelial Nerve Modeling Demonstrated in Large Animal Airway Tissue. (a,b) Top, oblique, and lateral projections of 3D nerve data alone and overlaid with computer modeling. (a) Guinea pig epithelial nerves (white) from trachea overlaid with the computer nerve model (green). (b) Epithelial nerves (white) and nerve modeling (green) demonstrated in canine airway tissue obtained using a forceps biopsy.

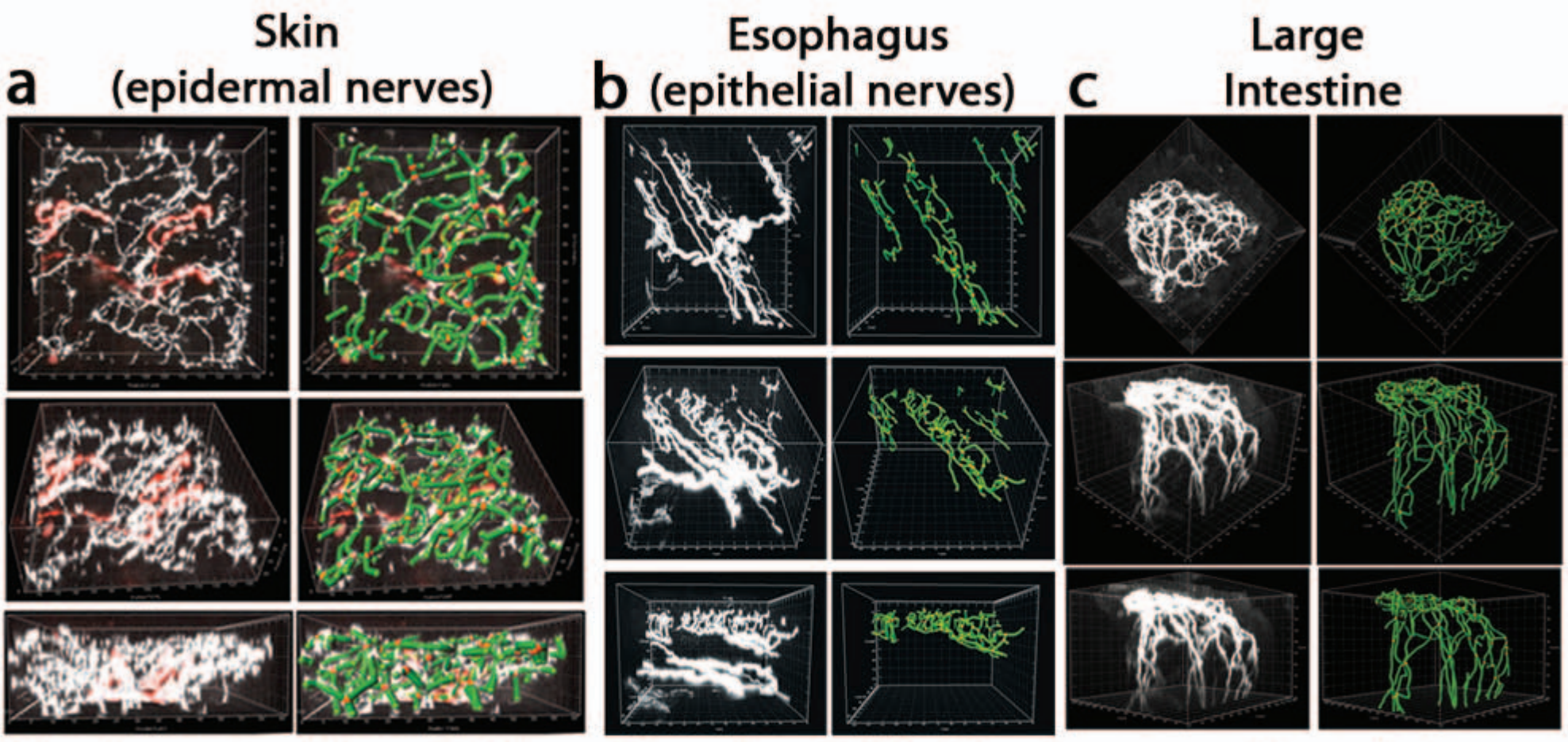

Supplementary Figure 8. Nerve Mapping in Skin, Esophagus, and Large Intestine. (a-c) Top, oblique, and lateral projections of nerve image data (white) alone, overlaid with the computer nerve map (green), or the nerve map alone. (a) Epidermal nerves (b) proximal esophageal epithelial nerves (c) intestinal nerves

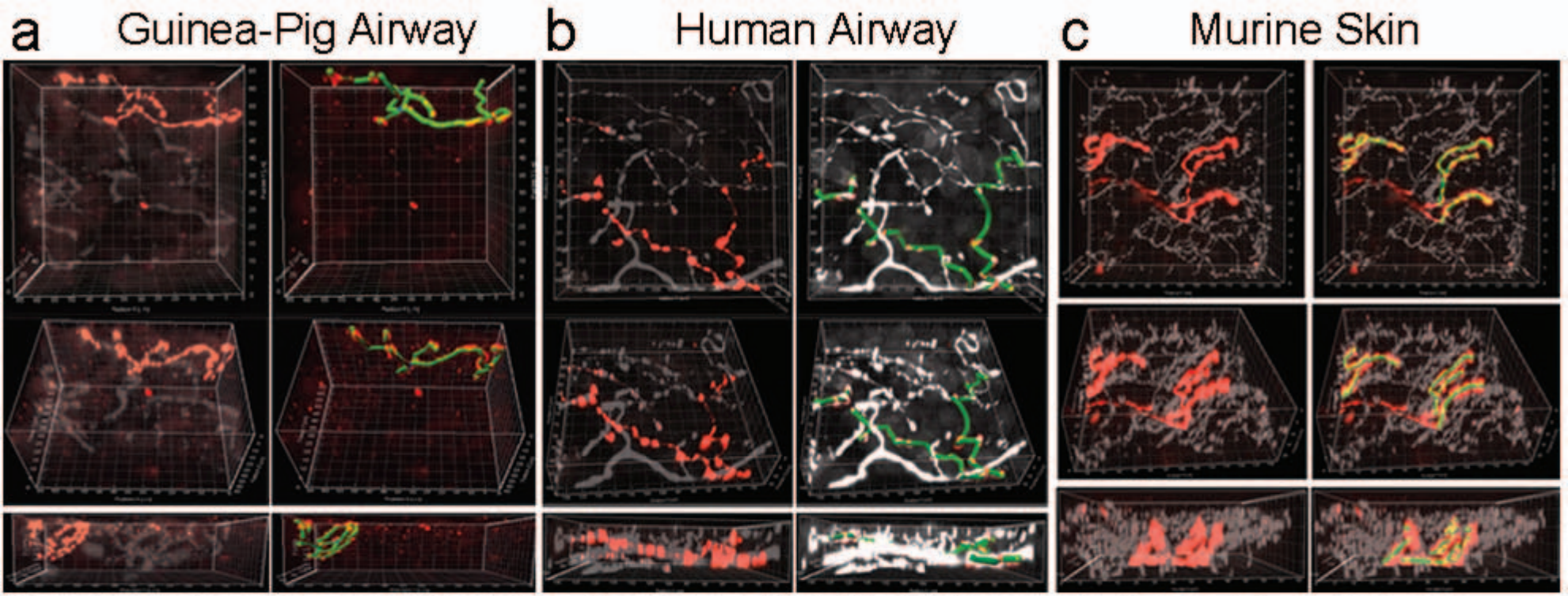

Supplementary Figure 9. Modeling Substance P Epithelial Nerves in Guinea Pig and Human Airway, and Mouse SkinTissue. (a-c) Top, oblique, and lateral projections of 3D nerve data alone and overlaid with computer modeling. All nerves (white - transparent) were labeled using the pan-neuronal marker, PGP 9.5, and a sub-population (red) labeled with an antibody against substance P. (a) Guinea pig tracheal epithelial nerves shown alone and overlaid with substance P nerve model. (b) Human epithelial nerves from forceps biopsy tissue (pan-neuronal staining shown in Figure 5) overlaid with the substance P nerve model. (c) Mouse epidermal nerves shown alone and overlaid with substance P nerve model

Human Trachea Columnar Epithelium

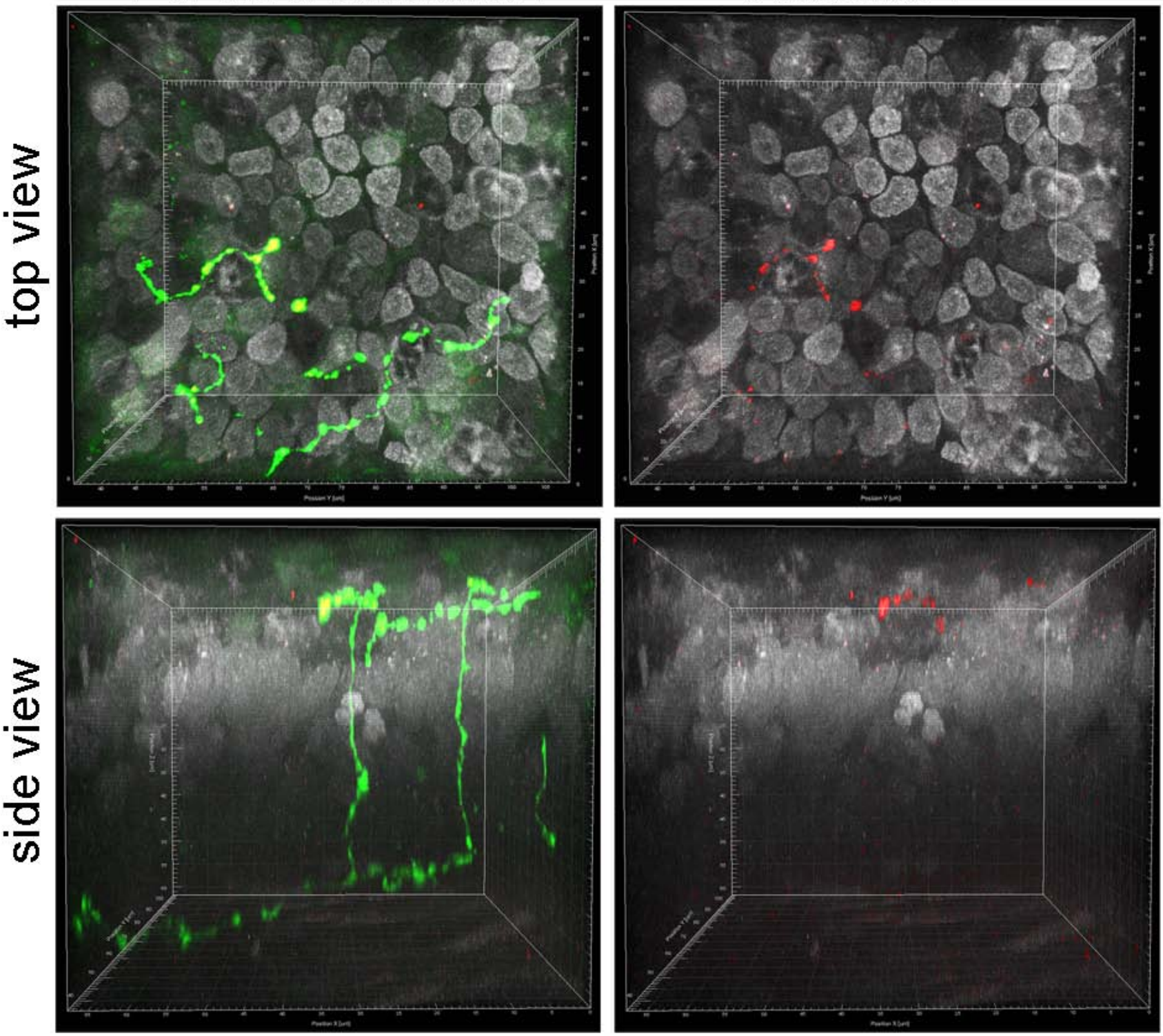

Supplementary Figure 10. Substance P Epithelial Nerves in Human Trachea Obtained At Autopsy. Top, oblique, and side projections of 3D nerve data. All nerves (green) were labeled using the pan-neuronal marker, PGP 9.5, and a sub-population (red) labeled with an antibody against substance P.